

# Theoretical Analysis of Composite RC Beams with Pultruded GFRP Beams subjected to Impact Loading

**Teghreed H. Ibrahim**

Department of Civil Engineering, University of Baghdad, Iraq  
tagreed.hassan@coeng.uobaghdad.edu.iq (corresponding author)

**Ihsan A. S. Alshaarba**

Civil Engineering Department, Al-Esraa University College, Iraq  
ishaarba@esraa.edu.iq

**Abbas A. Allawi**

Department of Civil Engineering, University of Baghdad, Iraq  
a.allawi@uobaghdad.edu.iq

**Nazar K. Oukaili**

Department of Civil Engineering, University of Baghdad, Iraq  
nazar.oukaili@coeng.uobaghdad.edu.iq

**Ayman El-Zohairy**

Department of Engineering and Technology, Texas A&M University-Commerce, TX, USA  
ayman.elzohairy@tamuc.edu

**AbdulMuttalab I. Said**

Department of Civil Engineering, University of Baghdad, Iraq  
dr.abdulmuttalib.i.said@coeng.uobaghdad.edu

*Received: 22 September 2023 | Revised: 8 October 2023 and 14 October 2023 | Accepted: 16 October 2023*

*Licensed under a CC-BY 4.0 license | Copyright (c) by the authors | DOI: <https://doi.org/10.48084/etasr.6424>*

## ABSTRACT

Glass Fiber Reinforced Polymer (GFRP) beams have gained attention due to their promising mechanical properties and potential for structural applications. Combining GFRP core and encasing materials creates a composite beam with superior mechanical properties. This paper describes the testing encased GFRP beams as composite Reinforced Concrete (RC) beams under low-velocity impact load. Theoretical analysis was used with practical results to simulate the tested beams' behavior and predict the generated energies during the impact loading. The impact response was investigated using repeated drops of 42.5 kg falling mass from various heights. An analysis was performed using accelerometer readings to calculate the generalized inertial load. The integrated acceleration record and the measured hammer load vs. time data were utilized to determine the generalized bending load and fracture energy. Four forms of energy were calculated at the maximum load. The total energy was calculated and divided into two parts: The first part was gained by the beam's rotational kinetic energy, the bending energy in the specimen, and the elastic strain energy. The second part was the hammer's kinetic energy before striking the beam. The analytical results showed that the bending energy was less than its rotational kinetic energy for the encased GFRP beams and the reference specimens. In contrast, the encased steel beams had high bending energy due to the higher impact load and deflection. Strain energy recorded lower energy values for all specimens with higher bending energy. There is a good agreement between the tested and the calculated inertial and bending force for all beams. The ratio of inertia force to the total impact load for the encased GFRP and encased steel beams to the reference beam is about 9% and 5%, respectively.

*Keywords-composite beam; GFRP; impact loading; inertial load; kinetic energy; energy-dispersive*

## I. INTRODUCTION

Encased GFRP beams consist of a GFRP I-section encased in a layer of concrete or another material to provide additional support and improve load-carrying capacity. Combining the GFRP core and the encasing material creates a composite beam with superior mechanical properties compared to traditional steel and concrete beams. The mechanical properties of encased GFRP beams, such as strength and stiffness, can vary depending on the properties of the GFRP core, the encasing material, and the bonding between the two materials. High-quality GFRP, encasing materials, and proper bonding techniques can lead to stronger and more durable beams. GFRP has a higher strength-to-weight ratio than steel or concrete, meaning it can carry more load per unit weight. This makes encased GFRP beams an attractive option for applications where weight is a concern. Another advantage of encased GFRP beams is their corrosion resistance. GFRP makes it ideal for use in harsh environments or structures exposed to moisture. Overall, encased GFRP beams show great promise as a lightweight, corrosion-resistant, and high-strength alternative to traditional steel and concrete beams. GFRP I-sections and GFRP bars are enhanced composite materials identified as potential new building materials. These materials may be used for RC in cases where the performance of steel reinforcement is insufficient, and corrosion of steel bars is one of the most life-limiting problems of building materials [1]. Although the GFRP bars offer more flexibility in design as they can be used as individual bars and can be easily cut and bent on-site to accommodate specific project requirements [2], the GFRP I-section shape offers a higher moment of inertia, making it more resistant to bending and capable of withstanding larger loads without excessive deflection. So, GFRP I-sections offer greater stiffness than GFRP bars due to their shape and design.

Numerous experiments have been carried out on the encased GFRP I-section to explore the impact of the location of the GFRP I-beam within the cross-section and of the type of longitudinal tensile bars (steel or GFRP bars) [3, 4]. The results of these experiments demonstrated that the suggested composite beams exhibit a ductile response and achieve a higher ultimate load than the reference beam without GFRP. Additionally, it was observed that the bottom flanges of the I-section, being more effectively utilized than the top flanges, retain good tensile strength even after reaching maximum load. Some slippage was noted between the concrete and the I-section, while the specific positioning of the I-section had minimal impact on the ultimate load of the test beams. However, when GFRP bars were used as reinforcements instead of tensile steel bars, there was a significant reduction in stiffness and ultimate load. This reduction can be attributed to the brittle failure of the GFRP bars, which adversely affected the ductility of the beam members [3]. Impact loading represents an extremely severe loading condition characterized by applying an intense force over a short duration. Previous researchers have indicated that when a structural element is subjected to an impact load, it elicits two distinct responses: a local response and a global response. The local response is primarily caused by the stress wave generated at the impact

point, whereas the global response arises from the subsequent elastic-plastic deformation over an extended period throughout the structural member [5-10]. The failure of RC beams under impact loading raises significant concerns, with localized failures such as penetration, scabbing, perforation, and punching shear being the most commonly observed types of failure in RC elements subjected to impact loads.

Various investigators have subjected different structural elements (e.g. flexural members, compression members, tension members, and slabs) to dynamic loadings [11]. The energy-absorbing capacities of the materials were investigated under various strain rate loadings. Many procedures have been used, including free-fall drop weight experiments, explosive testing, Charpy or Izod tests, Hopkinson split bar tests, and fracture mechanics. However, previous tests of this type were not fully instrumented. It is now recognized that essential data can be lost without proper instrumentation [11]. Most of these tests were designed to determine "work of fracture" or "toughness" values [9]. The primary material properties, such as the constitutive laws in compression or tension, critical stress intensity factors, and critical strain energy release rates, were also attempted to be obtained. As a result, RC beams were predicted to behave differently at different loading rates. The first dynamic tests on concrete in compression were conducted in 1917, and many more have been worked on over the last 50 years [13]. Some researchers have discovered that inertial loading slightly affects impact testing. Thus, a considerable portion of the top load is needed to accelerate the specimen from rest at the beginning of the impact event. Therefore, not all of the top load acts as the bending stress on the model. This effect is known as "inertial loading" [14]. Authors in [11] tested normal and high-strength RC beams, and the results showed that concrete is a very strain-rate-sensitive material. Also, the dynamic load increases the peak bending loads and fracture energy. Using time-step integration, a beam's response to a pulse from the outside was modeled, whereas the model predicted concrete's nonlinear behavior under impact loading.

To predict what happens theoretically when a foreign object strikes a composite structure, four mathematical models were used in [15]: spring-mass models, energy-balance models, complete models, and an impact on an infinite plate model. Simple models are easy to use and work well, but they have limitations because they are based on simplifying assumptions. The impact dynamics can be understood by analyzing the system's energy balance. The projectile's initial kinetic energy was used to deform the structure during impact. Assuming the structure is quasi-static, the projectile's velocity becomes zero when it reaches its maximum deformation [15]. Authors in [6] studied the reactions of RC beams subjected to impact. They developed an analytical model to predict the mid-span's maximum deflection and impact load. In their experimental investigation, drop hammer impact test was employed to explore the influence of drop height and longitudinal steel reinforcement on reinforced concrete beams. The failure modes observed in reinforced concrete beams under impact loads were found to be dependent on the presence of longitudinal reinforcement. Specifically, reinforced concrete beams with

relatively less longitudinal steel reinforcement exhibited overall flexural failure due to the concentrated loading at a single point [6]. Authors in [16] tested 12 beams with GFRP coating, subjected to different loading rates. The virtual work principle was utilized to obtain a generalized inertial load from the measured hammer specimen, which allowed determining the actual bending load on the specimens. The results indicated that the ultimate load capacity of RC beams increased as the loading rate intensified. Furthermore, using externally bonded fiber-reinforced polymer sheets proved highly effective in enhancing the resistance of RC beams to impact loading. Author in [17] examined the low-velocity impact characteristics of GFRP laminated composites with thickness varying from 2 to 8 mm. The primary purpose of this research was to investigate the low-velocity impact response on FRP laminates and how they behave when damaged by thoroughly understanding the main damage processes based on impact force and peak energies. Authors in [18] indicated that using stiffeners on the GFRP composite beams has a clear effect on increasing the strength of the composite beams and damping time under the impact load. At the same time, it reduced the damping ratio due to the increased vibration duration induced by increasing the compressive strength of concrete. They also noted that secondary crushing and the concrete's non-linear behavior caused the profiles to collapse after absorbing more than 45% of the load. Authors in [19] studied the flexural behavior of encased GFRP I-beams under static load and indicated that using the GFRP section of composite beams improved their strength by more than 50%. In [22], the authors investigated the impact behavior of encased pultruded I-GFRP and I-steel RC beams. The impact loading performance of composite beams was studied using verified Finite Element (FE) models, and it has been found that the concrete compressive strength significantly impacts the beams' performance. Increasing the concrete's compressive strength effectively altered the impact parameters of the RC composite specimens with GFRP I-beams. The maximum impact load was raised by an average of 18% to 25% across all specimens when the compressive strength was 35 MPa. At 45 MPa, compressive strength was in the 30–40% range [20].

The current study analyzed the test results of impact loading at varying impact velocities for dropped objects using theoretical analysis for the performance of composite RC beams constructed from GFRP and steel beams. From the measured acceleration and impact load data, the generalized inertial and bending loads were calculated. Moreover, the total energy was calculated in four forms: rotational kinetic energy, bending energy in the specimen, elastic strain energy, and the kinetic energy of the hammer before striking the beam.

## II. EXPERIMENTAL PROGRAM

### A. Test Matrix

A testing program involving fabricating, casting, and testing 4 simply supported RC composite beams with Pultruded GFRP beams of 3000 mm overall length and 2750 mm clear span was carried out to explore the flexural performance of these structural members under impact loading [20]. The cross sections of the beams along the spans were kept uniform at 300 mm in depth and 200 mm in width [20]. The tested beams were

reinforced with longitudinal steel rebars of 16 mm and 10 mm diameter at the bottom and top, respectively, of the cross-section. Transverse reinforcement was provided with 10 mm diameter stirrups at 125 mm spacing throughout the entire spans of the tested beams. Embedded steel I-beam and pultruded GFRP beam were used compositely with the concrete beams by excluding the reference beam. These embedded sections were centered at the centroid axes of the concrete cross-section. Moreover, their lengths were identical to the concrete beams'. The following symbols were adopted for the tested beam according to the assumed parameters: NR-I for the reference beam reinforced with longitudinal steel rebars only, CG-I for the beam with embedded pultruded GFRP I-beam, CGC-I for the beam with embedded pultruded GFRP I-beam and shear connectors, and CS-I for the beam with embedded steel I-beam [20]. Shear connectors of 12 mm diameter and 70 mm height were used to improve the composite contact between the pultruded beam and concrete. They were distributed in two rows at 375 mm longitudinal spacing along the top flange of the GFRP beams through predrilled holes. Washers and nuts were tightened around the shear connector above and below the drilled holes to achieve good connections between the shear connectors and the top flange of the pultruded beam.

### B. Material Properties

The concrete mechanical properties, such as compressive strength, splitting tensile strength, modulus of rupture, and modulus of elasticity, were determined using concrete specimens. After one day of casting, all specimens were demolded and the curing process was conducted by using damp canvas and continuous water soaking to ensure a good curing treatment for 28 days. Three concrete cubes with dimensions of 150 mm × 150 mm × 150 mm and three 150 mm × 300 mm cylinders were prepared and tested to determine the compressive strength of the concrete according to BS1811-116-11 [21] and ASTM C 39/C 39M-18 [22], respectively. The splitting tensile strength of concrete was calculated by testing a standard concrete cylinder (150 mm × 300 mm) following ASTM C496 / C496M-17[23]. A typical concrete prism (500 mm × 100 mm × 100 mm) was tested to determine the concrete modulus of rupture according to ASTM C78-22 [24]. Furthermore, a standard concrete cylinder (300 mm × 150 mm) was tested to determine the concrete's modulus of elasticity according to ASTM C469-14 [25]. On the other hand, ASTM A370-22 [26] was used to evaluate the mechanical properties of steel bars and steel plates, where 3 bars of 10 mm and 16 mm in diameter and a gauge length of 500 mm and two steel plates with flat coupons were tested. Compressive and tensile strengths and the elastic modulus of the GFRP I-beam were studied. For the compressive test, 15 coupon 10 mm × 12.7 mm × 38.1 mm specimens were prepared and tested according to ASTM D695-15 [27]. While for tensile tests, 15 coupon specimens with dimensions of 10 mm × 25 mm × 250 mm were tested according to ISO 527 [28]. The average results of all the tests are listed in Table I.

### C. Test Setup and Instrumentations

The impact tests were carried out on the beams using a three-point loading scheme with effective spans of 2750 mm.

The test setup can be seen in Figures 1-2. The hammer's mass was 42.5 kg, representing one-tenth of the tested beam's mass. This mass was dropped repeatedly on the top surface of the tested beam at mid-span from 5 different heights: 250 mm, 500 mm, 1000 mm, 1500 mm, and 1900 mm. During testing, a hoist consisting of an electric winch and steel rope was used to displace the impacting hammer and the falling mass to a certain height over the tested beam. Once the hammer reached the required position, the hoist was detached manually from the hammer. Upon release, the hammer fell under gravity through steel guide rails, stroke the tested beam, and generated high-stress loading. The load was transferred from the impacting hammer to the beam directly. The displacement boundary conditions of the tested specimens include using simple supports with supplementary steel yokes to allow free rotation, restrain the vertical translation, and prevent twisting at both ends of the beam.

TABLE I. MATERIAL PROPERTIES

| Material    | Diameter (mm) | Thickness (mm) | Yield strength (MPa) | Compressive strength (MPa) | Tensile strength (MPa) | Modulus of elasticity (GPa) |
|-------------|---------------|----------------|----------------------|----------------------------|------------------------|-----------------------------|
| Concrete    | -             | -              | -                    | 23.4                       | 2.4                    | 20.75                       |
| Steel bar   | 16            | -              | 520.7                | -                          | 687.0                  | 200                         |
|             | 10            | -              | 407.7                | -                          | 465.6                  | 200                         |
| Steel plate | -             | 10             | 375.9                | -                          | 479.6                  | 200                         |
| GFRP        | -             | 10             | -                    | 326.1                      | 347.5                  | 27.1                        |

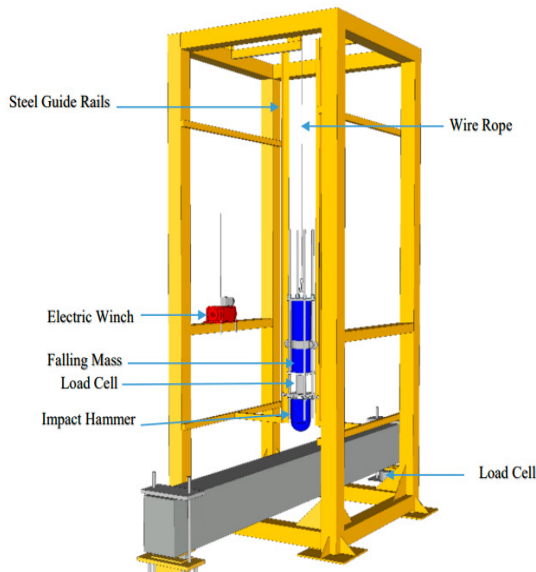


Fig. 1. Test setup for the impact loading.

Two load cells were used to record the impact loading while striking the specimen. The falling mass system was rigidly connected to a dynamic load cell (the first load cell) between the impacting hammer and steel shaft. To measure the vertical support reaction, a 1000 kN load cell (the second load cell) was installed beneath one of the supports. For each stepped time, the deflection response at the mid-span of the tested beams was recorded using a laser deflection sensor type LK-081 and its controller. The laser deflection sensor had a measuring range of 150 mm. An accelerometer was attached to

the upper surface of the dynamic load cell to measure the impactor's acceleration. Three other accelerometers were attached at the top surface of the beam to measure beam acceleration. One of the accelerometers was placed at 50 mm from the mid-span section, and the other two were placed at 688 mm and 1375 mm from the mid-span section, respectively. The instrumentations were connected to a data recorder type DATAQ DI-710 (see Figure 3).

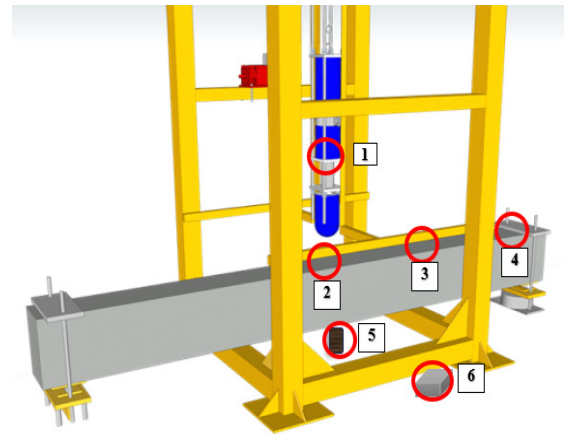


Fig. 2. Instrumentation. 1. Accelerometer located at the upper surface of the dynamic load cell to measure the acceleration of the impactor, 2. accelerometer at 50 mm from the beam center, 3. accelerometer at 688 mm from the beam center, 4. accelerometer at 1375 mm from the beam center, 5. laser deflection sensor, 6. laser sensor controller.

### III. EXPERIMENTAL RESULTS

#### A. Impact Response

Impact loads and deflection time histories were recorded for the 5 heights of 250 mm, 500 mm, 1000 mm, and 1900 mm, as listed in Table II. Figure 3 displays the typical results for specimen NR-I. The behavior of a structural component subjected to impact loading was divided into 2 response phases: the local response caused by stress wave at the loading point and the overall response generated by elastic-plastic deformation that occurs over a long period in the whole structural member following impact as presented in [4, 5]. All tested beams' maximum impact force increased as the drop height increased. The ultimate impact force of beam CS-I was 130% greater than that of reference beam BR for a drop height of 1900 mm. Maximum impact forces for beams CG-I and CGC-I at the same drop height were 19% and 77% of the reference beam, respectively. The steel beam's higher stiffness caused the difference in the behavior compared to the GFRP beam, as impact force is proportional to structural element stiffness. The first pulse's peak increased proportionately to the drop height in the mid-span deflection time histories, whereas the initial pulse-like waveform lasted about 25 ms regardless of drop height. Although the length of the blunt waveform increased with drop height, the peaks were approximately independently of the drop height. The maximum mid-span deflection increased as the drop height increased. Figures 4 and 5 compare the maximum impact force and mid-span deflection for various drop heights.

TABLE II. IMPACT TEST RESULTS

| Specimen | Height of drop (mm) | Total impact force $P_i$ (kN) | Tested support force (kN) | Bending force $P_b$ (kN) | Inertia force $P_i$ (kN) | Mid-span deflection (mm) |
|----------|---------------------|-------------------------------|---------------------------|--------------------------|--------------------------|--------------------------|
| NR-I     | 250                 | 28.52                         | 12.63                     | 25.26                    | 3.26                     | 1.20                     |
|          | 500                 | 30.21                         | 14.50                     | 29.00                    | 1.21                     | 1.80                     |
|          | 1000                | 43.02                         | 20.02                     | 40.04                    | 2.98                     | 2.00                     |
|          | 1500                | 66.53                         | 32.03                     | 64.06                    | 2.47                     | 2.60                     |
|          | 1900                | 95.82                         | 45.87                     | 91.74                    | 4.08                     | 2.70                     |
| CG-I     | 250                 | 46.79                         | 22.09                     | 44.18                    | 2.61                     | 1.09                     |
|          | 500                 | 62.83                         | 28.36                     | 56.72                    | 6.11                     | 1.59                     |
|          | 1000                | 86.58                         | 40.40                     | 80.80                    | 5.78                     | 1.95                     |
|          | 1500                | 95.32                         | 45.27                     | 90.54                    | 4.78                     | 2.39                     |
|          | 1900                | 113.98                        | 54.27                     | 108.54                   | 5.44                     | 2.41                     |
| CGC-I    | 250                 | 33.25                         | 15.20                     | 30.40                    | 2.85                     | 1.01                     |
|          | 500                 | 42.70                         | 20.30                     | 40.60                    | 2.10                     | 1.20                     |
|          | 1000                | 68.57                         | 33.40                     | 66.80                    | 1.77                     | 1.95                     |
|          | 1500                | 107.56                        | 51.10                     | 102.20                   | 5.36                     | 2.13                     |
|          | 1900                | 169.79                        | 80.67                     | 161.34                   | 8.45                     | 2.32                     |
| CS-I     | 250                 | 63.72                         | 30.68                     | 61.36                    | 2.36                     | 1.23                     |
|          | 500                 | 111.96                        | 53.78                     | 107.55                   | 4.41                     | 2.10                     |
|          | 1000                | 142.81                        | 66.76                     | 133.52                   | 9.29                     | 2.34                     |
|          | 1500                | 195.61                        | 85.66                     | 171.33                   | 24.28                    | 3.04                     |
|          | 1900                | 221.24                        | 98.79                     | 197.58                   | 23.66                    | 3.92                     |

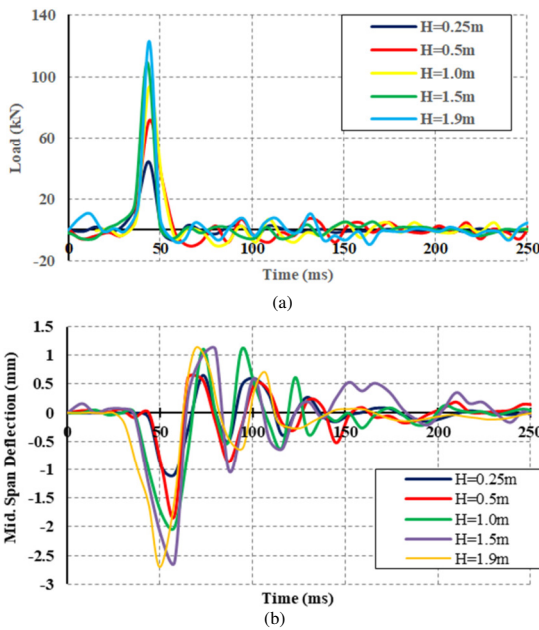


Fig. 3. The impact loads and deflection time histories for beam NR-I. (a) Load-time history, (b) deflection-time history.

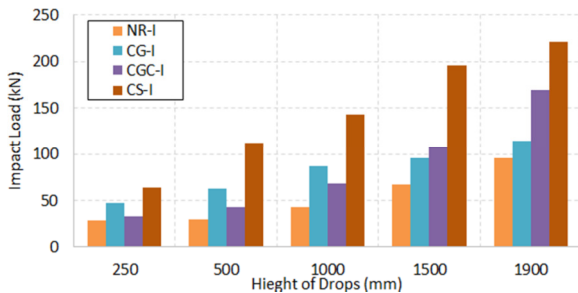


Fig. 4. Maximum impact force comparisons for various drop heights.

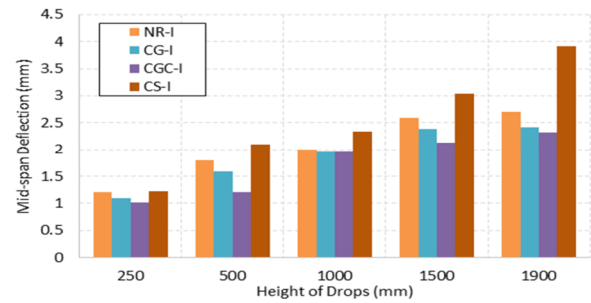


Fig. 5. Maximum mid-span deflection comparisons for various drop heights.

B. Accelerations

Figure 6 illustrates the measured accelerations vs. time for the drop height of 1900 mm for the tested beams. These results were recorded using the accelerometers placed at 50 mm, 688 mm, and approximately 1375 mm from the impact location. The peak acceleration values were between 30 and 40 m/s<sup>2</sup> and the time of the peak acceleration was the same as the peak impact load. In the case of NR-I beam, acceleration rapidly decreased following the peak and dissipated entirely after approximately 200 ms. Preliminary tests on the acceleration distribution may show that it can be assumed as a sinusoidal distribution (Figure 6). For NR-I, CG-I, and CGC-I specimens, the acceleration distribution decreased gradually from the mid-span to the support end. In contrast, the response of acceleration for CS-I at the location of 688 mm from the beam center was different due to the high stiffness of this beam.

IV. THEORETICAL ANALYSIS OF THE RESULTS

The impact loads, support reactions, and accelerations at 3 locations along the tested beams were the main output of the impact loading tests (Figure 2). The results were collected as functions of time. The data were collected at 250 ms intervals, whereas an impact event could take anywhere from 30 to 150 ms. To properly analyze the results, it is significant to distinguish between the inertia and total loads. Due to the inertial reaction of the beam under test, the bending force on the beam is not equal to the contact load between the beam and the hammer. In the early stages of an impact, the inertial load can be much more than the load absorbed in bending the beam. Since only a tiny percentage of the total weight bends the beam, the whole load is highly sensitive to the inertia effect [29].

A. Inertial and Total Loads

The generalized inertial load  $P_i(t)$  was calculated using the accelerations measured by the accelerometers placed on the beam to determine the contribution of the inertia load to the total load measured by the hammer,  $P_t(t)$ . Consider a sinusoidal displacement distribution and the following parameters to estimate  $P_i(t)$ :  $u(x,t)$  represents the beam displacement inside the supports,  $u(y,t)$  is the beam displacement at the sections overhanging the supports,  $\rho$  is the mass density of the beam material,  $u_0(t)$  is the displacement in the beam's center,  $\ddot{u}_0(t)$  is the acceleration in the beam's center,  $A$  is the area of the beam cross-section, and  $\delta u_0(t)$  is the virtual displacement at the beam's center, consistent with the boundary conditions (Figure 8).

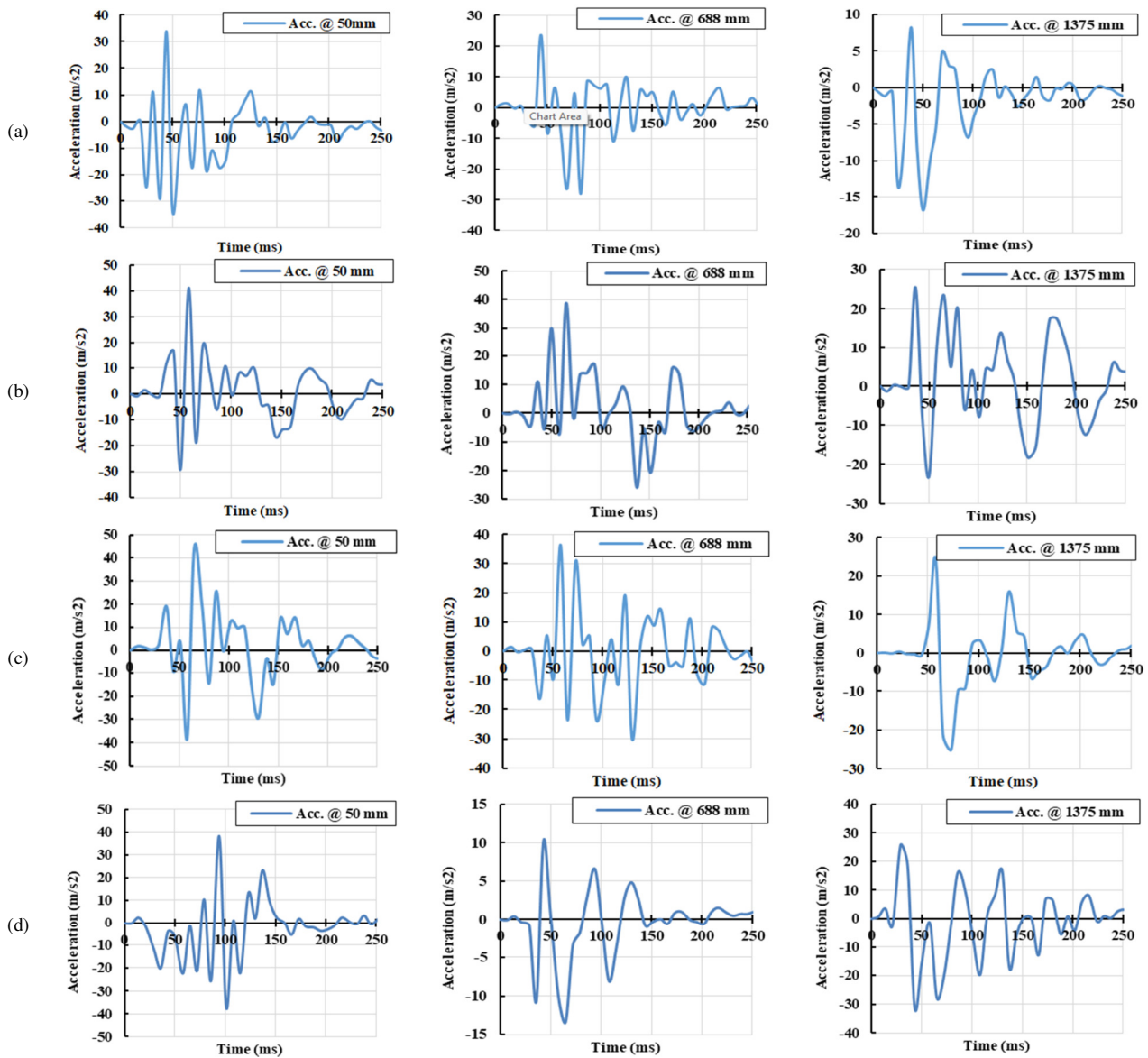


Fig. 6. Acceleration time histories for the drop height of 1900 mm at different locations for (a) NR-I, (b) CG-I, (c) CGC-I, and (d) CS-I beams.

As a result, displacements along the beam and between the supports were assumed to be sinusoidal. In contrast, displacements in the beam's overhanging regions were supposed to be linear. As a result, the displacements between supports and in overhanging regions, respectively, can be written down as:

$$u(x,t) = u_0(t) \sin \frac{\pi x}{l} \tag{1}$$

$$u(y,t) = \frac{-u_0(t)\pi}{l} y \tag{2}$$

The inertial load along the beam's length is represented by the generalized inertial load  $P_i(t)$ . At the mid-span of the beam, a virtual displacement of  $u_0$  was assumed. In this configuration, the generalized inertial load  $P_i(t)$  should perform the same amount of virtual work as the distributed inertial forces:

$$P_i(t)\delta u_0 = \int_0^l \rho A \left( \ddot{u}_0(t) \sin \frac{\pi x}{l} \right) \left( \delta u_0 \frac{\sin \pi x}{l} \right) dx + 2 \int_0^h \rho A \left( \frac{-\ddot{u}_0(t)\pi y}{l} \right) \left( \frac{-\delta u_0 \pi y}{l} \right) dy \tag{3}$$

Equation (3) can be simplified further for a prismatic homogeneous beam as follows:

$$P_i(t) = \rho A \ddot{u}_0(t) \left[ \frac{l}{2} + \frac{2\pi^2 h^3}{l^2 \cdot 3} \right] \tag{4}$$

The beam was modeled as a single-degree-of-freedom system after finding the generalized inertial load, and the generalized bending load may be obtained using the equation of dynamic equilibrium:

$$P_b(t) = P_t(t) - P_i(t) \tag{5}$$

where  $P_t(t)$  is the observed hammer load and  $P_b(t)$  is the bending load on the beam.

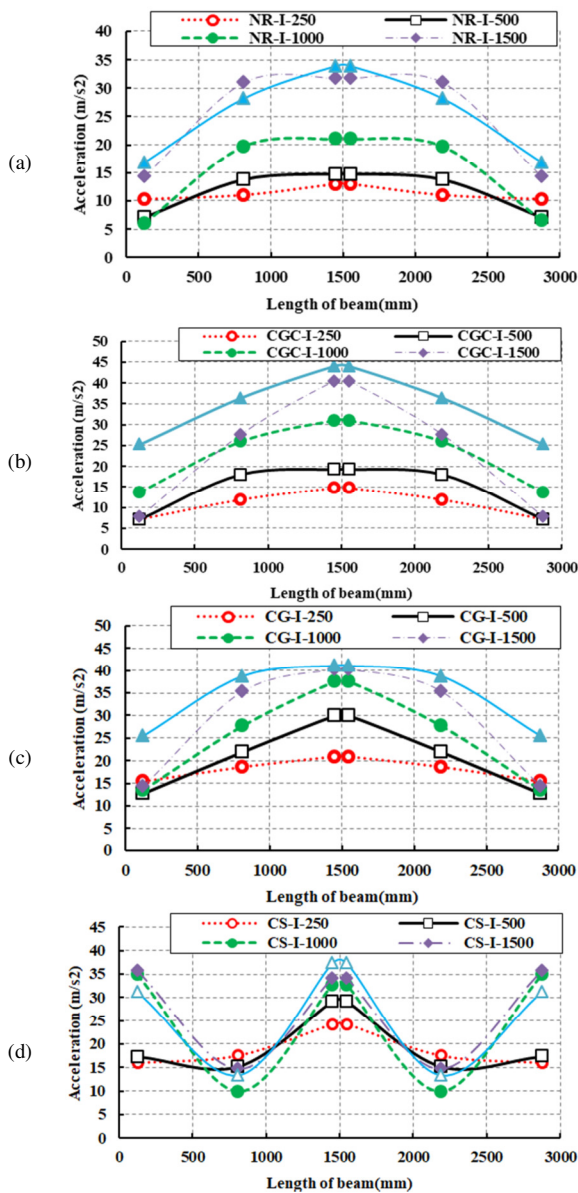


Fig. 7. Acceleration distribution along specimens for different drop heights.

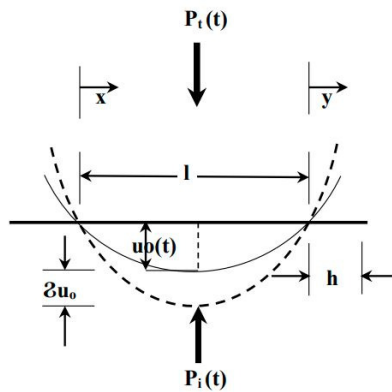


Fig. 8. The sinusoidal acceleration distribution along the beam.

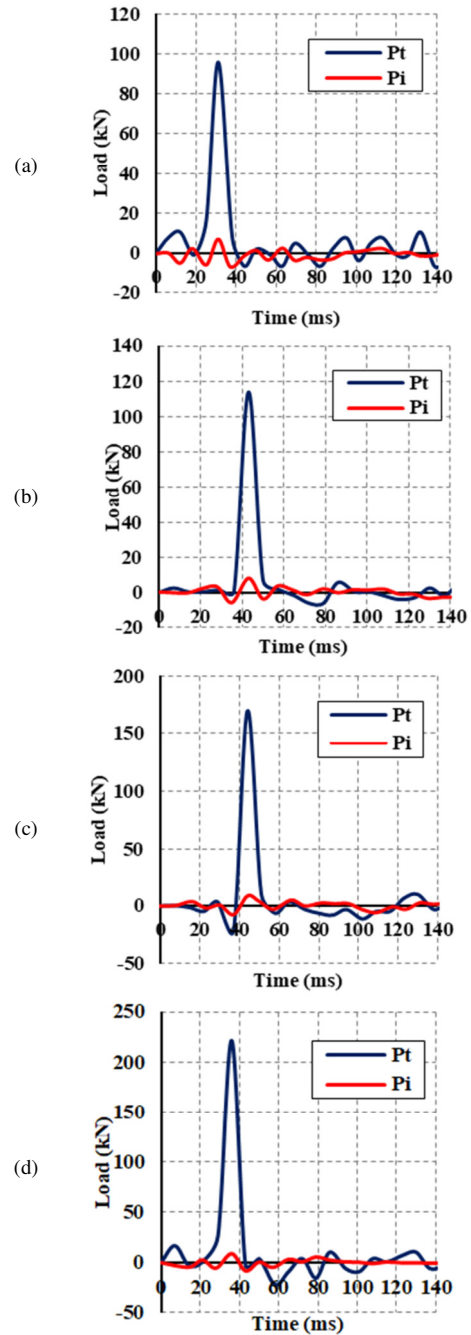


Fig. 9. Total hammer load and inertial load time history for the drop height of 1900 mm. (a) NR-I, (b) CG-I, (c) CGC-I, and (d) CS-I beams.

Figure 9 depicts the total load measured by the hammer as well as the calculated inertia load versus time for a drop height of 1900 mm. In this figure, the contribution of the inertial load was about 10% of the total hammer load for beams NR-I, CG-I and CGC-I, while it was 5% for beam CS-I, respectively. The results for all the drop heights are compared in Table III. The inertial load increased as the drop height increased due to the change in the loading rate with a nearly linear variation. The contribution of the inertia force from the total impact load is about 9% for the NR-I, CG-I, and CGC-I beams and about 5%

for the CS-I beam. Stiffer systems appeared to experience lower accelerations and, as a result, developed lower inertial loads compared to the more miniature rigid beams [11]. Therefore, the composite beams showed greater inertial loads relative to the reference beam [31]. Figure 10 compares the

tested and calculated inertial and bending forces with approximately identical values for the NR-I, CG-I, and CGC-I specimens and slight differences for the CS-I specimen. The bending load was significant at the drop height of 1900 mm for all tested beams, as can be seen in Figure 10.

TABLE III. SUMMARY FOR THE INERTIAL AND BENDING LOADS FOR ALL BEAMS AND DROP HEIGHTS

| Specimen | Drop height (mm) | Tested max. mid-span deflection (mm) | Tested impact (total) force (kN) | Acceleration at 50 mm (m/s <sup>2</sup> ) | Calculated inertial force (kN) | Calculated bending force (kN) | Ratio of inertial force to total force (%) |
|----------|------------------|--------------------------------------|----------------------------------|---|--------------------------------|-------------------------------|--|
| NR-I     | 250              | 1.2                                  | 28.52                            | 13.02                                     | 2.66                           | 25.86                         | 9.34                                       |
|          | 500              | 1.8                                  | 30.21                            | 14.79                                     | 3.02                           | 27.19                         | 10.01                                      |
|          | 1000             | 2                                    | 43.02                            | 21.02                                     | 4.30                           | 38.72                         | 9.99                                       |
|          | 1500             | 2.6                                  | 66.53                            | 31.74                                     | 6.49                           | 60.04                         | 9.75                                       |
|          | 1900             | 2.7                                  | 95.82                            | 33.90                                     | 6.93                           | 88.89                         | 7.23                                       |
| CG-I     | 250              | 1.09                                 | 46.79                            | 20.90                                     | 4.27                           | 42.52                         | 9.13                                       |
|          | 500              | 1.59                                 | 62.83                            | 29.92                                     | 6.12                           | 56.71                         | 9.74                                       |
|          | 1000             | 1.95                                 | 86.58                            | 37.52                                     | 7.67                           | 78.91                         | 8.86                                       |
|          | 1500             | 2.39                                 | 107.56                           | 40.25                                     | 8.23                           | 99.33                         | 7.65                                       |
|          | 1900             | 2.41                                 | 169.79                           | 41.14                                     | 8.41                           | 161.38                        | 4.95                                       |
| CGC-I    | 250              | 1.01                                 | 33.25                            | 14.77                                     | 3.02                           | 30.23                         | 9.08                                       |
|          | 500              | 1.2                                  | 42.70                            | 19.28                                     | 3.94                           | 38.76                         | 9.23                                       |
|          | 1000             | 1.95                                 | 68.57                            | 31.02                                     | 6.34                           | 62.23                         | 9.25                                       |
|          | 1500             | 2.13                                 | 95.32                            | 40.49                                     | 8.28                           | 87.04                         | 8.69                                       |
|          | 1900             | 2.32                                 | 113.98                           | 44.03                                     | 9.00                           | 104.98                        | 7.90                                       |
| CS-I     | 250              | 1.23                                 | 63.72                            | 24.21                                     | 4.95                           | 58.77                         | 7.77                                       |
|          | 500              | 2.1                                  | 111.96                           | 29.09                                     | 5.95                           | 106.01                        | 5.31                                       |
|          | 1000             | 2.34                                 | 142.81                           | 32.59                                     | 6.66                           | 136.15                        | 4.67                                       |
|          | 1500             | 3.04                                 | 195.61                           | 34.02                                     | 6.96                           | 188.65                        | 3.56                                       |
|          | 1900             | 3.92                                 | 221.24                           | 37.27                                     | 7.62                           | 213.62                        | 3.45                                       |

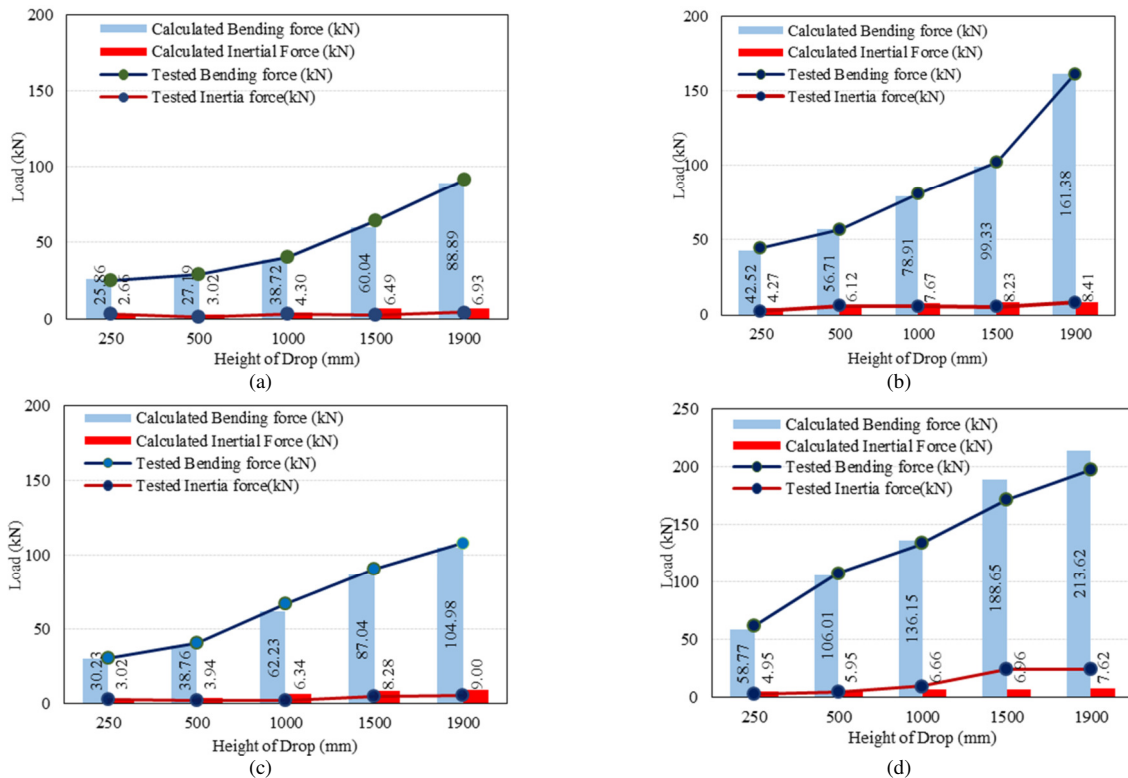


Fig. 10. Comparison between the tested and the calculated inertial and bending forces. (a) NR-I, (b) CG-I, (c) CGC-I, and (d) CS-I beams.

B. Energies

The energy balance theory compares the energy the beam gains and the energy the hammer loses at each impact point using the energy conservation principle. Considering no losses in the system, the energy conservation law dictates that these two energies are equal [11]. Various approaches were examined to address the dissipation of hammer energy in a drop-weight-type impact machine. As the hammer descends, its downward momentum is diminished upon striking the beam. Just before the hammer makes contact with the beam, its velocity and kinetic energy can be expressed as:

$$v = \sqrt{2a_h h} \tag{6}$$

$$E_k = \frac{1}{2} m_h v^2 = m_h a_h h \tag{7}$$

where  $m_h$  represents the hammer's mass,  $a_h$  denotes the acceleration of the hammer, and  $h$  represents the height of the hammer drop. The energy possessed by the hammer can be transferred to the beam through various mechanisms, including the energy consumed by the beam at peak load ( $t_p$ ). These energies can be in different forms, such as rotational kinetic energy  $E_{ker}(t_p)$  and beam bending energy  $E_b(t_p)$ . The bending energy in the beam comprises elastic strain energy  $E_{se}(t_p)$  and the work of fracture  $E_{wof}$ . Furthermore, this energy can be expressed as the area beneath the load vs. the mid-span displacement curve.

$$E_b(t_p) = \int P_b(t) du_o \tag{8}$$

The elastic strain energy  $E_{se}(t_p)$  can be calculated precisely from the load vs. center point displacement plot by calculating the secant modulus at the peak load (see Figure 11). Because the load vs. deflection curve became noticeably non-linear at this point, the secant modulus was calculated as shown in (9):

$$E_{se}(t_p) = 0.6 P_b(t_p) u_{oe} \tag{9}$$

where  $u_{oe}$  represents the elastic component of the midspan displacement. The bending energy is subtracted from the strain energy to determine the fracture work. The rotating kinetic energy can be determined by (10), which involves integration over the length of the specimen and the assumption of a linear velocity distribution along the beam's length.

$$E_{ker}(t) = \frac{8\rho A u_o^2(t)}{l^2} \left[ \frac{l^3}{24} + \frac{h^3}{3} \right] \tag{10}$$

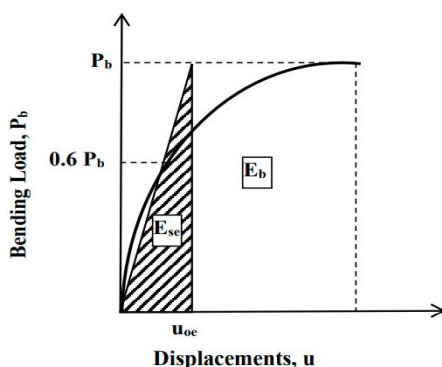


Fig. 11. Components of the bending energy.

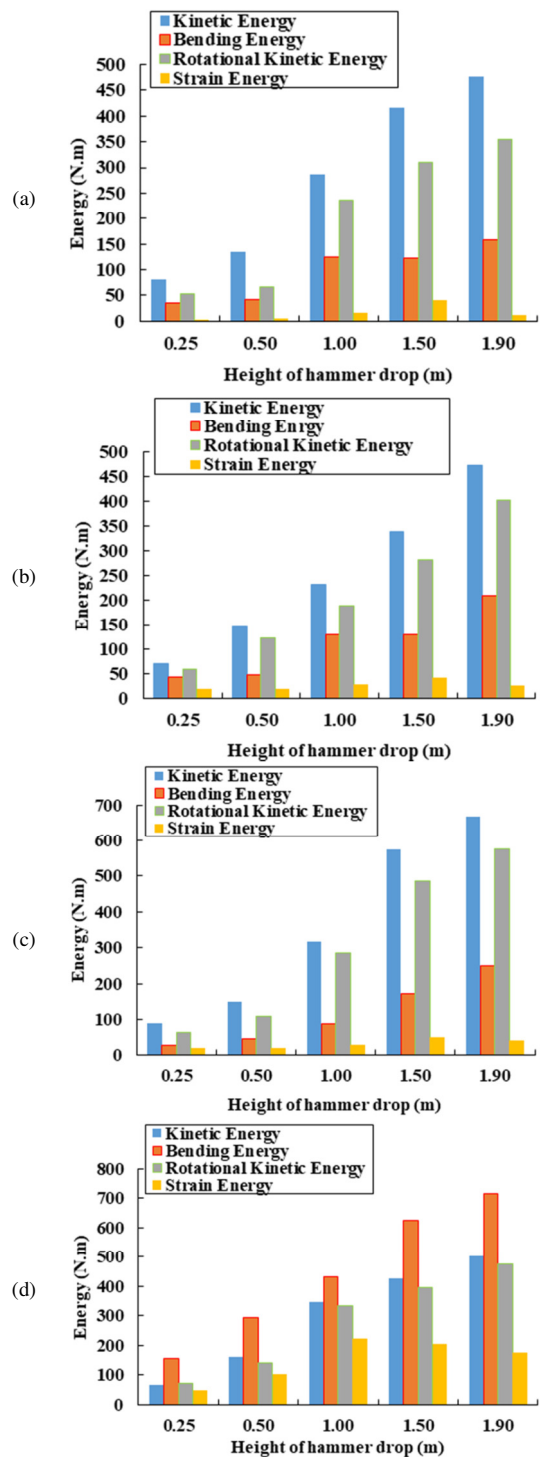


Fig. 12. Energies at the impact for all drop heights. (a) NR-I, (b) CG-I, (c) CGC-I, and (d) CS-I beams.

The hammer's momentum is quickly transferred to the beam when it strikes it. As a result, the hammer's momentum was reduced. The momentum ( $M$ ) is calculated by [30]:

$$M = m.v \tag{11}$$

This reduces the kinetic energy of the hammer while increasing the energy of the beam. The rapid transfer of energy between the hammer and the beam causes a rapid buildup of stress in the beam. Kinetic energy and momentum increase with the height of the hammer fall, which rises drop velocity, which is directly proportional to kinetic energy and momentum, but momentum increases linearly with velocity, whereas kinetic energy increases quadratically. Hence, their quantities are always different at higher levels of velocity.

Figure 12 illustrates the four forms of energy for all beams. At the peak load, the total energy was divided into two types: the energy gained by the beam ( $E_{ker}$ ,  $E_b$ , and  $E_{se}$ ) and the second energy of the hammer before striking the beam ( $E_k$ ). Some quantity of the energy is thought to be absorbed during the striking process as vibrations and stored elastic energy. The energy gained by the beam by its deformed shape ( $E_b$ ) was less than the rotational kinetic energy ( $E_{ker}$ ) for specimens NR-I, CG-I, and CGC-I, but it was more significant for CS-I due to the higher impact load and deflection. All models had lower energy values for strain energy, which was part of the bending energy.

## V. CONCLUSIONS

This paper describes the testing of composite RC beams with pultruded GFRP and steel beams under low-velocity impact loading. Theoretical analysis was used along with the practical results to simulate the tested beams' behavior and predict the generated energies during the impact loading. The impact responses were investigated using repeated drops of 42.5 kg falling mass from various heights. The performed analysis considered accelerometer readings to calculate the generalized inertial load. Based on the experimental and theoretical results, the following conclusions can be drawn:

- The acceleration distribution decreased gradually from the mid-span to the support end. In contrast, the response of acceleration for CS-I at 688 mm from the beam center was different due to the higher stiffness of the steel beam.
- The change in the loading rate caused the hammer's drop height to be successfully raised, which increased the inertial force.
- The calculated inertial force for the composite models is much higher than the reference specimen's.
- The contribution of the inertia force from the total impact load is about 9% for the reference and encased GFRP beams and about 5% for the encased steel beam.
- The bending energy was smaller than its rotational kinetic energy for the encased GFRP beams and the reference beam. In contrast, the composite beam with a steel profile exhibited higher bending energy because of the higher impact load and deflection.

## REFERENCES

- [1] H. H. Ali and A. M. I. Said, "Flexural behavior of concrete beams with horizontal and vertical openings reinforced by glass-fiber-reinforced polymer (GFRP) bars," *Journal of the Mechanical Behavior of Materials*, vol. 31, no. 1, pp. 407–415, Jan. 2022, <https://doi.org/10.1515/jmbm-2022-0045>.
- [2] M. A. E. Zareef, "An Experimental and Numerical Analysis of the Flexural Performance of Lightweight Concrete Beams reinforced with GFRP Bars," *Engineering, Technology & Applied Science Research*, vol. 13, no. 3, pp. 10776–10780, Jun. 2023, <https://doi.org/10.48084/etasr.5871>.
- [3] M. N. S. Hadi and J. S. Yuan, "Experimental investigation of composite beams reinforced with GFRP I-beam and steel bars," *Construction and Building Materials*, vol. 144, pp. 462–474, Jul. 2017, <https://doi.org/10.1016/j.conbuildmat.2017.03.217>.
- [4] M. N. S. Hadi and J. Youssef, "Experimental Investigation of GFRP-Reinforced and GFRP-Encased Square Concrete Specimens under Axial and Eccentric Load, and Four-Point Bending Test," *Journal of Composites for Construction*, vol. 20, no. 5, Oct. 2016, Art. no. 04016020, [https://doi.org/10.1061/\(ASCE\)CC.1943-5614.0000675](https://doi.org/10.1061/(ASCE)CC.1943-5614.0000675).
- [5] A. Q. Bhatti, N. Kishi, H. Mikami, and T. Ando, "Elasto-plastic impact response analysis of shear-failure-type RC beams with shear rebars," *Materials & Design*, vol. 30, no. 3, pp. 502–510, Mar. 2009, <https://doi.org/10.1016/j.matdes.2008.05.068>.
- [6] K. Fujikake, B. Li, and S. Soeun, "Impact Response of Reinforced Concrete Beam and Its Analytical Evaluation," *Journal of Structural Engineering*, vol. 135, no. 8, pp. 938–950, Aug. 2009, [https://doi.org/10.1061/\(ASCE\)ST.1943-541X.0000039](https://doi.org/10.1061/(ASCE)ST.1943-541X.0000039).
- [7] N. K. A. Oukaili and A. Al Shammari, "Impact Response of Reinforced Concrete T-Beams with Multiple Web Opening And Its Theoretical Simulation," in *Second International Conference on Science, Engineering and Environment*, Osaka, Japan, Nov. 2016, pp. 234–240.
- [8] N. K. Oukaili and M. M. Khattab, "Serviceability and ductility of partially prestressed concrete beams under limited cycles of repeated loading," *International Journal of GEOMATE*, vol. 17, no. 60, pp. 9–15, Nov. 2021, <https://doi.org/10.21660/2019.60.4514>.
- [9] A. N. Hassooni and S. R. A. Zaidee, "Behavior and Strength of Composite Columns under the Impact of Uniaxial Compression Loading," *Engineering, Technology & Applied Science Research*, vol. 12, no. 4, pp. 8843–8849, Aug. 2022, <https://doi.org/10.48084/etasr.4753>.
- [10] J. Abd and I. K. Ahmed, "The Effect of Low Velocity Impact Loading on Self-Compacting Concrete Reinforced with Carbon Fiber Reinforced Polymers," *Engineering, Technology & Applied Science Research*, vol. 11, no. 5, pp. 7689–7694, Oct. 2021, <https://doi.org/10.48084/etasr.4419>.
- [11] N. P. Banthia, "Impact resistance of concrete," Ph.D. dissertation, University of British Columbia, Vancouver, BC, Canada, 1987.
- [12] A. A. Allawi, "Behavior of Strengthened Composite Prestressed Concrete Girders under Static and Repeated Loading," *Advances in Civil Engineering*, vol. 2017, Dec. 2017, Art. no. e3619545, <https://doi.org/10.1155/2017/3619545>.
- [13] D. A. Abrams, "Effect of Rate of Application of Load on the Compressive Strength of Concrete," *Proceeding of ASTM*, vol. 17, pp. 364–377, 1917.
- [14] B. Cotterell, "Fracture Toughness and the Charpy V Notch Impact Test," *British Welding Association*, vol. 9, no. 2, pp. 83–90, 1962.
- [15] S. Abrate, "Modeling of impacts on composite structures," *Composite Structures*, vol. 51, no. 2, pp. 129–138, Feb. 2001, [https://doi.org/10.1016/S0263-8223\(00\)00138-0](https://doi.org/10.1016/S0263-8223(00)00138-0).
- [16] S. M. Soleimani and N. Banthia, "Reinforced Concrete Beams under Impact Loading and Influence of a GFRP Coating," *International Journal of Civil Engineering*, vol. 1, pp. 68–77, Mar. 2010.
- [17] C. Evci, "Thickness-dependent energy dissipation characteristics of laminated composites subjected to low velocity impact," *Composite Structures*, vol. 133, pp. 508–521, Dec. 2015, <https://doi.org/10.1016/j.compstruct.2015.07.111>.
- [18] A. A. Allawi and S. I. Ali, "Flexural Behavior of Composite GFRP Pultruded I-Section Beams under Static and Impact Loading," *Civil Engineering Journal*, vol. 6, no. 11, pp. 2143–2158, Nov. 2020, <https://doi.org/10.28991/cej-2020-03091608>.
- [19] T. H. Ibrahim, A. A. Allawi, and A. El-Zohairy, "Experimental and FE analysis of composite RC beams with encased pultruded GFRP I-beam under static loads," *Advances in Structural Engineering*, vol. 26, no. 3, pp. 516–532, Feb. 2023, <https://doi.org/10.1177/13694332221130795>.

- [20] T. H. Ibrahim, A. A. Allawi, and A. El-Zohairy, "Impact Behavior of Composite Reinforced Concrete Beams with Pultruded I-GFRP Beam," *Materials*, vol. 15, no. 2, Jan. 2022, Art. no. 441, <https://doi.org/10.3390/ma15020441>.
- [21] *ASTM C39/C39M-18(2018), Standard Test Method for Compressive Strength of Cylindrical Concrete Specimens*. West Conshohocken, PA, USA: ASTM International, 2018.
- [22] *BS1811-116-11: Method for determination of compressive strength of concrete cubes*. BSI, 2011.
- [23] *ASTM C496/C496M-17(2017), Standard Test Method for Splitting Tensile Strength of Cylindrical Concrete Specimens*. West Conshohocken, PA, USA: ASTM International, 2017.
- [24] *ASTM C78/C78M-22(2022), Standard Test Method for Flexural Strength of Concrete (Using Simple Beam with Third-Point Loading)*. West Conshohocken, PA, USA: ASTM International, 2022.
- [25] *ASTM C469/C469M-14(2014), Standard Test Method For Static Modulus Of Elasticity And Poisson's Ratio Of Concrete In Compression*. West Conshohocken, PA, USA: ASTM International, 2014.
- [26] *ASTM A370-22(2022), Standard Test Methods And Definitions For Mechanical Testing Of Steel Products*. West Conshohocken, PA, USA: ASTM International, 2022.
- [27] *ASTM D695-15(2015), Standard Test Method for Compressive Properties of Rigid Plastics*. West Conshohocken, PA, USA: ASTM International, 2015.
- [28] *ISO 527-5:2021. Plastics Determination of tensile properties Part 5: Test conditions for unidirectional fibre-reinforced plastic composites*. ISO, 2021.
- [29] A. Bentur, S. Mindess, and N. Banthia, "The behaviour of concrete under impact loading: Experimental procedures and method of analysis," *Materials and Structures*, vol. 19, no. 5, pp. 371–378, Sep. 1986, <https://doi.org/10.1007/BF02472127>.
- [30] A. I. Said and E. M. Mouwainea, "Behaviours of reinforced concrete slabs under static loads and high-mass low velocity impact loads," *IOP Conference Series: Materials Science and Engineering*, vol. 1067, no. 1, Oct. 2021, Art. no. 012036, <https://doi.org/10.1088/1757-899X/1067/1/012036>.
- [31] M. C. Liejy *et al.*, "Prediction of the Bending Strength of a Composite Steel Beam–Slab Member Filled with Recycled Concrete," *Materials*, vol. 16, no. 7, Jan. 2023, Art. no. 2748, <https://doi.org/10.3390/ma16072748>.